Boundary-Layer Meteorol manuscript No.
(will be inserted by the editor)

Pollutant Dispersion in a Developing Valley Cold-Air Pool

Charles Chemel · **Paul Burns**

Submitted: 13 November 2013 / Revised: 29 May 2014 (R1), 3 October 2014 (R2), 28 October 2014 (R3)

Abstract Pollutants are trapped and accumulate within cold-air pools, thereby affecting air quality. A numerical model is used to quantify the role of cold-air-pooling processes in the dispersion of air pollution in a developing cold-air pool within an alpine valley under decoupled stable conditions. Results indicate that the negatively buoyant downslope flows transport and mix pollutants into the valley to depths that depend on the temperature deficit of the flow and the ambient temperature structure inside the valley. Along the slopes, pollutants are generally entrained above the cold-air pool and detrained within the cold-air pool, largely above the ground-based inversion layer. The ability of the cold-air pool to dilute pollutants is quantified. The analysis shows that the downslope flows fill the valley with air from above, which is then largely trapped within the cold-air pool, and that dilution depends on where the pollutants are emitted with respect to the positions of the top of the ground-based inversion layer and cold-air pool, and on the slope wind speeds. Over the lower part of the slopes, the cold-air-pool-averaged concentrations are proportional to the slope wind speeds where the pollutants are emitted, and diminish as the cold-air pool deepens. Pollutants emitted within the ground-based inversion layer are largely trapped there. Pollutants emitted farther up the slopes detrain within the cold-air pool above the ground-based inversion layer, although some fraction, increasing with distance from the top of the slopes, penetrates into the ground-based inversion layer.

Keywords Cold-air pools · Downslope flows · Numerical simulation · Pollutant dispersion

1 Introduction

Cold-air pools (CAPs) in regions of hilly and mountainous terrain refer to layers of cold air confined towards the bottom of landscape depressions (see, for instance, Whiteman 2000).

C. Chemel (✉)
National Centre for Atmospheric Science (NCAS), Centre for Atmospheric & Instrumentation Research (CAIR), University of Hertfordshire, College Lane, Hatfield, AL10 9AB, UK
e-mail: c.chemel@herts.ac.uk

P. Burns
Centre for Atmospheric & Instrumentation Research (CAIR), University of Hertfordshire, College Lane, Hatfield, AL10 9AB, UK

CAPs frequently occur during nocturnal hours and the winter season in basins and poorly-drained valleys decoupled from the atmosphere above, which is the case considered herein. Previous work has considered the case of coupled conditions where larger-scale non-local flows (e.g. synoptic weather systems) perturb the complex terrain atmosphere (e.g. Vosper and Brown 2008; Whiteman et al. 2010; Dorninger et al. 2011; Haiden et al. 2011; Lareau and Horel 2014). The mechanisms by which the atmosphere cools in complex terrain under decoupled stable conditions have been discussed in several observational and modelling studies (see Zardi and Whiteman 2013, for a review, and references therein). However, much remains to be understood about the relative roles of turbulent and radiative flux divergences and advection. Vosper et al. (2014) discussed results from a numerical model simulation of the formation of a CAP in early March 2010 in the Clun Valley, United Kingdom, a narrow valley with depth between 75 and 150 m, using horizontal grid spacings of 100 m and a vertical grid resolution of 2 m close to the ground surface. Results of the simulation indicated that parametrized subgrid-scale turbulent mixing dominates the cooling of the air adjacent to the ground while the cooling above is dominated by the advection of cold air away from the surface into the interior valley atmosphere.

Burns and Chemel (2014a,b) analyzed results from a numerical simulation of a developing region of enhanced cooling (referred to as CAP thereafter, for simplicity) in an idealized 1-km deep narrow U-shaped valley at the latitude of the Chamonix valley, France. This terrain is in contrast with the small-scale terrain considered in the works cited above, as well as the case of much larger basin landforms that have also been investigated (e.g. Cuxart and Jiménez 2007; Martínez and Cuxart 2009; Martínez et al. 2010). Burns and Chemel (2014a,b) used horizontal grid spacings of 30 m and a vertical grid resolution of about 1.5 m adjacent to the ground. The simulation started about 1 h before sunset on a winter day. After 1 h of relatively rapid valley-atmosphere cooling, driven mainly by radiative cooling, the cooling rate of the valley atmosphere decreased during the simulated 8-h period as a result of a complex balance/interplay between radiation and dynamical effects (Burns and Chemel 2014a). Within 1 h following sunset, the valley-atmosphere instantaneous cooling was almost equally partitioned between dynamics (i.e., advection and subgrid-scale turbulent mixing) and radiative cooling. Burns and Chemel (2014b) investigated the interactions between the downslope flows and the developing CAP. As the CAP deepened, a 100-m deep strongly stratified ground-based inversion layer was left above the valley floor. As the developing CAP engulfed the slopes, the downslope flows within the CAP could not maintain their negative buoyancy by losing heat to the underlying surface, and detrained into the developing CAP, largely above the ground-based inversion layer, thereby mixing the CAP atmosphere.

Much research has been devoted to improving understanding of the dispersion of air pollution in complex terrain and much progress has been made. A number of previous studies have focused on daytime conditions or have considered daily-averaged quantities. Chazette et al. (2005) documented the vertical distribution of ozone, nitrogen oxides and aerosols in the Chamonix valley, France, during daylight hours on winter days when a strongly stratified ground-based inversion layer had developed during the night or persisted throughout the day. Pollutants were found to be trapped near their sources within the inversion layer (observed to be 150 ± 50-m deep), thereby affecting air quality, and to be essentially isolated from the air above. Such trapping of pollutants close to the ground surface was observed, during morning hours of winter days, in the Inn valley, Austria (Harnisch et al. 2009; Schnitzhofer et al. 2009), and in the Adige valley, Italy (de Franceschi and Zardi 2009). Lehner and Gohm (2010) used an idealized numerical simulation to investigate the daytime tracer transport in the Inn valley. Prolonged multi-day episodes of high daily-averaged aerosol concentrations have been observed close to the ground during winter in the Cache valley, Utah, USA

(Malek et al. 2006). The pollution events were well correlated with the presence of ground-based stable layers. Silcox et al. (2012) reported observations of elevated daily-averaged aerosol concentrations during days with persistent, multi-day CAPs in the Salt Lake valley, Utah, USA. Aerosol concentrations were found to be linearly correlated with the valley heat deficit, a measure of the overall atmospheric stability within the valley. Under most conditions, atmospheric stability increased with time during CAP events, causing air pollution to intensify from sources within the ground-based inversion layer. Hence, the highest concentrations were usually found in the longest lasting CAPs. Concentrations were generally observed to decrease with increasing elevation, with decreases in ground-level concentrations of up to 30 % for differences in elevation of about 300 m.

Previous investigations of nocturnal air pollution in complex terrain have frequently used near-ground point samples and (quasi-) vertical profiles, often focusing on the ground-based inversion layer. Raga et al. (1999) described the occurrence of high near-ground ozone concentrations at night in the Mexico City basin, Mexico, due to the return of ozone-rich air, carried by downslope flows, following the advection of pollution above the basin by daytime upslope winds. A similar effect was observed by King et al. (1987) who released tracers over the slopes of the Los Angeles basin, California, USA. Lee et al. (2003) reported similar events in the Phoenix valley, Arizona, USA, when the lower layers of the valley atmosphere were weakly stratified. However, when a strongly stratified ground-based inversion layer developed, downslope flows detrained near the top of the growing inversion layer.

The full spatial and temporal variations of pollutants during CAP events remain to be examined, presumably owing to the challenges in modelling CAPs (Baker et al. 2011) and making extensive observations of CAPs. The present study builds on previous research by explicitly studying the dispersion of air pollution within an alpine valley during nocturnal hours, under decoupled poorly-drained conditions. The work quantifies how the complex interactions between the downslope flows and the developing region of enhanced cooling, studied by Burns and Chemel (2014a,b), affect the dispersion of pollutants emitted at different locations over the slopes of the valley. The region of enhanced cooling includes both the ground-based inversion and the region of enhanced cooling that expands above this layer. The design of the numerical experiment is presented in Sect. 2, numerical results are analyzed in Sect. 3, and a summary follows in Sect. 4.

2 Design of the numerical experiment

The numerical simulation presented herein was performed with the Weather Research and Forecasting (WRF) model (Skamarock et al. 2008), version 3.4.1, run in a large-eddy simulation (LES) mode (i.e., with no boundary-layer parametrization scheme). The WRF model was set-up exactly as in Burns and Chemel (2014a) with the inclusion of additional prognostic passive tracers (referred to as pollutants), governed by the tracer-conservation equation

$$\frac{\partial C_i}{\partial t} + \mathbf{u}\cdot\nabla C_i = \frac{1}{\rho}\nabla\cdot(\rho\,\kappa\nabla C_i) + Q_i, \qquad (1)$$

where C_i is the concentration (volume mixing ratio) of pollutant P_i, $\mathbf{u}$ is the velocity field, ρ is the air density, κ is the eddy diffusivity for heat and mass, and Q_i is the source emission rate of pollutant P_i. A turbulent kinetic energy 1.5-order closure scheme (Deardorff 1980) was used to model the subgrid scales. The constant C_k in the subgrid-scale parametrization scheme was set to 0.10 (see Moeng et al. 2007). Also, because of the anisotropy of the grid, the width of the spatial filter was modified in the present simulation following Scotti et al.

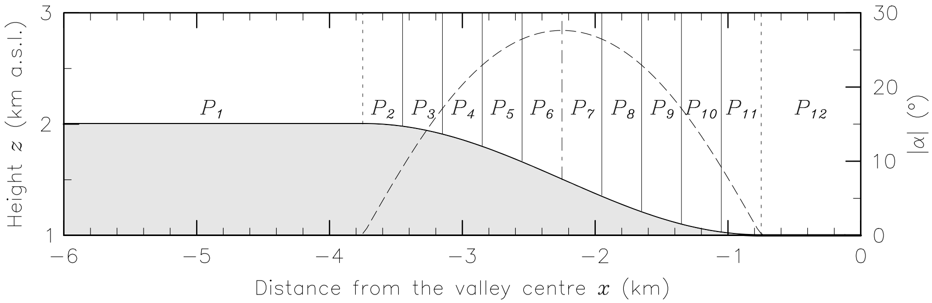

Fig. 1 Terrain height (curved solid line) along the x-direction orientated west-east. The terrain is symmetric about $x = 0$ and uniform in the along-valley direction y (into the page), orientated south-north, though the domain extends 1.2 km in the y-direction. The dashed line indicates the absolute value of the slope angle $|\alpha|$. The vertical dotted lines mark the top and bottom of the slopes and the vertical dashed-dotted line marks the slope inflection point, which is located half-way along the slopes. The regions where the pollutants P_i, $i \in [1..12]$, are emitted within the model layer adjacent to the ground are also indicated (see text for details).

(1993). A brief summary of the model set-up is given below. Dynamics and physics options are not detailed hereafter and the reader is referred to Burns and Chemel (2014a).

The model domain encompasses an idealized deep narrow U-shaped valley, with its axis orientated south-north in the y-direction (see Fig. 1). All points in the domain are located at 45.92 °N and 6.87 °E, corresponding to the location of the Chamonix valley, France, and the size of the valley approximates that of the lower Chamonix valley. It is 1 km deep and flanked on either side by a horizontal plateau extending 2.25 km from the top of the valley slopes. The width of the valley floor is 1.5 km, the slopes are about 3.2 km long and the maximum slope angle is 27.6°. The terrain is uniform in the along-valley direction y, though the domain extends 1.2 km in this direction. The model top is located at 12 km above sea level (a.s.l.).

The two-dimensional terrain and the absence of any large-scale pressure differences along y mean that the simulation avoids the additional complexity of along-valley winds. The simulation considers the case of poorly-drained valleys. McKee and O'Neal (1988) presented observations of both very weak and strong along-valley winds in different valleys. Analytical theory was used to demonstrate that the different wind speeds can be explained by different down-valley changes in the width to (cross-sectional) area ratio W/A of the valleys, neglecting any variation in the surface energy budgets. Valleys with W/A increasing down the valley lead to increasing cooling rates in the down-valley direction, leading to the formation of cooler air further down the valley, which effectively blocks the down-valley flow. McKee and O'Neal (1988) demonstrated that the magnitude of the forcing mechanism outlined above (termed the intra-valley force) can exceed the magnitude of forces due to mountain-plain temperature differences or due to temperature differences caused by sloping valley floors.

The domain is discretized using a terrain-following grid of type Arakawa-C with 101 staggered grid points along the z-direction, pointing upwards, with a vertical grid resolution Δz of about 1.5 m adjacent to the ground surface, stretching continuously to the model top using a hyperbolic tangent function. Δz was selected, on the basis of a sensitivity study, to capture the downslope flows. The horizontal grid resolution Δx is 30 m, resulting in 402 and 42 staggered grid points in the x- and y-directions, respectively. Δx was selected as a compromise between minimizing errors in the approximations of horizontal gradients due to grid distortion (Mahrer 1984) and keeping the runtime practical. The even number of horizontal grid points makes the model grid symmetric about its mass points.

The numerical model simulated an 8-h period, starting about 1 h before sunset at time $t = 0$ on a winter day (21 December). To obtain numerically stable results, the vertical grid resolution and maximum flow speed demanded a model timestep $\Delta t = 0.05$ s. The acoustic timestep was set to $\Delta t/10$. Given the steep slopes of the valley considered herein, the model parameter β, used to damp vertically propagating sound waves, was set to 0.9 (see Dudhia 1995).

Since we consider decoupled stable conditions, no synoptic forcing was prescribed at the initial time, that is, the velocity field was set to zero across the domain. The initial model atmosphere was weakly stratified, with a lapse rate in virtual potential temperature, $\partial\theta_v/\partial z = 1.5$ K km^{-1}, corresponding to an environmental lapse rate slightly less than the adiabatic rate. This initial state is typical of conditions where there is no pre-existing residual layer, or inversions, in the valley atmosphere at the start of the night, indicative of well-mixed post-convective conditions. Whiteman et al. (1997) and Whiteman and Zhong (2008) provide examples of such near-adiabatic lapse rates in complex terrain close to sunset. The near-surface air at the valley floor was assigned an initial $\theta_v = 288$ K, a temperature of approximately 279.3 K (about 6 °C), typical 1 h before sunset at this time of year in the Chamonix valley. This temperature value was taken from the Pollution in Alpine Valleys (POVA) dataset (see Brulfert et al. 2005; Burns and Chemel 2014a).

The atmosphere was initialized with a constant relative humidity of 40 %, corresponding to a relatively dry atmosphere, which avoided the complexity of cloud formation, while allowing for the expected overall slight reduction in water vapour with height due entrainment of drier air from above during daytime and evapotranspiration from the surface. It is acknowledged that large variations in water content can occur in the atmosphere and that this moisture profile is a particular and idealized case. Hoch et al. (2011) used a three-dimensional radiative transfer model to demonstrate that large variations in the water content in the atmosphere of valleys of different sizes (similar in scale and temperature structure to that considered herein) affect the magnitude of the valley-atmosphere instantaneous radiative cooling rates. Increasing the water vapour mass mixing ratio from 3.25 to 4.875 g kg^{-1} (that is a 50 % increase) increased the cooling rates by approximately 17 %. The effects of different initial moisture profiles should be quantified in future work, and the possibility of cloud and fog formation also needs to be considered in future work. At the same time, cloud formation generally reduces heat loss from the complex terrain atmosphere at night (Cuxart and Jiménez 2012), which has implications, for instance, for agriculture.

Periodic lateral boundary conditions were used. This was made possible by the relatively large extent of the flat plateaux in the x-direction, the symmetry of the domain about the centre of the valley, the y-independent valley geometry and largely y-independent forcing at the ground surface. A 4-km deep implicit Rayleigh damping layer (Klemp et al. 2008) was implemented at the top of the model domain to prevent any significant wave reflections affecting the solution. The damping coefficient was set to 0.2 s^{-1}. Forcing at the ground surface was provided by the revised MM5 Monin-Obukhov surface-layer scheme by Jiménez et al. (2012) coupled to the community Noah land-surface model (Chen and Dudhia 2001). The idealized terrain was set-up to represent an Alpine landscape consisting mainly of short grasses and the soil type was set to 'silty clay loam'. Setting the land-use type to short grass avoided placing the lowest layer of the model grid within the vegetation, which would have rendered the surface-layer parametrization inappropriate. Although many valleys are wooded, an accurate consideration of forested slopes would require the implementation of a new parametrization scheme in the WRF model, which is beyond the scope of the present work. The initial soil moisture was set constant at a value 10 % below the soil's field capacity [0.387 (volume fraction)], simulating soil conditions a few days after rainfall. This is reasonable given the winter period modelled, when frequent precipitation is typical in the Alps. For a detailed account of the initialization of the soil temperature and moisture, see Burns and Chemel (2014a). The skin temperature was initialized by second-order extrapolation of the air temperature at the first three layers above the ground.

The initial atmospheric and surface conditions avoided the complexity of dewfall or frostfall during the simulated period. Whiteman et al. (2007) demonstrated that these processes can significantly reduce the atmosphere cooling rates within small-scale landscape depressions. Whiteman et al. (2007) made tethered balloon soundings in the Gruenloch basin, Austria, a depression with a width and depth of approximately 1 km and 150 m, respectively. The basin atmosphere water vapour mixing ratio fell by 2–3 g kg^{-1} overnight, resulting in a latent heat release that was 33–53 % of the overall basin sensible heat loss. Theory was used to indicate that the effects of dewfall and frostfall are less during winter, when ambient air temperatures are lower. It is unclear whether dewfall and frostfall have such a large impact in larger-scale topography, such as that considered herein. A random negative thermal perturbation, with a minimum value of -0.05 K, was applied to the skin temperature at the initial time across the valley slopes to make the flow three-dimensional and reduce the spin-up time of the simulation.

Pollutants were emitted within the model layer adjacent to the ground surface on the plateaux (pollutant P_1), equally-spaced strips along the slopes (pollutant P_i, $i \in [2..11]$) and the valley floor (pollutant P_{12}). The regions where the pollutants are emitted are indicated in Fig. 1, noting that the surface areas S_i of these regions are different. Each pollutant P_i was emitted from the start of the simulation at a constant rate R_i ($= \rho\, Q_i \Delta z / M$, where M is the molar mass of air) such that $R_i S_i = 1.845 \times 10^{-5}$ mol s^{-1}. In this way, the same mass of pollutant was emitted for each pollutant. The initial volume mixing ratio for all the pollutants was set to 1 pptv to provide a constant background against which concentrations can be compared. The along-valley-averaged volume mixing ratio of pollutant P_i is denoted by C_i hereafter for simplicity and its deviation from the constant background is denoted by C_i'.

We consider the dispersion characteristics of passive tracers, which over the length and time scale considered, can reasonably be expected to represent the trends of pollutant concentrations for species such as carbon monoxide.

3 Results and discussion

3.1 Dispersion characteristics of the downslope flows

Figure 2 presents an overview of the along-valley-averaged downslope flow, its forcing mechanisms and dispersion characteristics along the western slope at time $t = 480$ min. Downslope flows develop as the result of ground-surface cooling along the slopes, which makes the air adjacent to the slopes negatively buoyant. The cooling of the slope surfaces is due to a net negative surface energy budget. The bottom two plots in Fig. 2 show the surface energy budget and the cooling rate at the ground surface. At that time, there is no shortwave radiation and the net longwave radiation budget is negative, leading to a cooling by radiative heat loss. The radiative deficit is most effectively replenished by conduction from the soil, warming the surface. The sensible heat flux is directed downwards, cooling the air adjacent to the surface, while the latent heat flux is directed upwards as a result of the availability of soil moisture for evaporation, cooling the surface. The residual ΔQ_S of the energy budget,

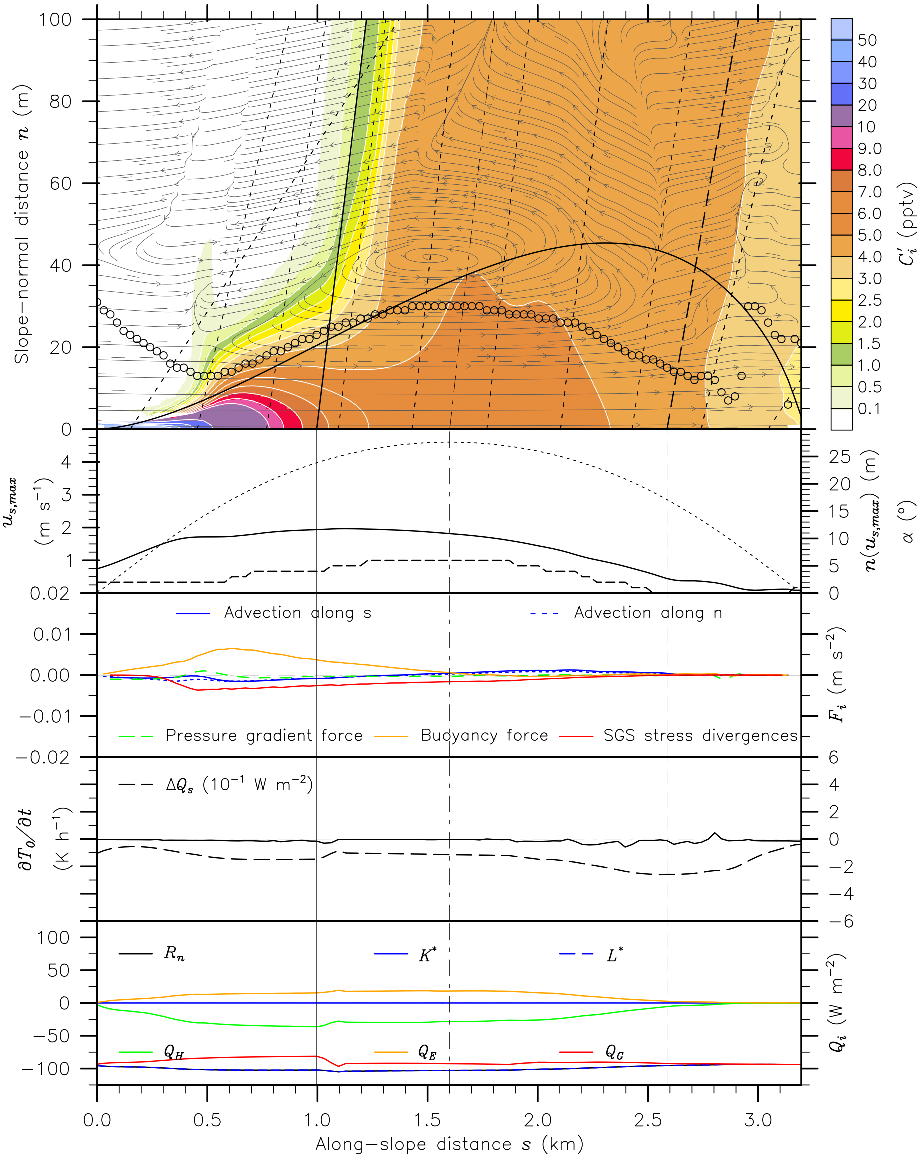

Fig. 2 Overview of the along-valley-averaged downslope flow, its forcing mechanisms and dispersion characteristics along the western slope at time $t = 480$ min. The top plot displays contours of the concentration C_1' of pollutant P_1, with streamlines superimposed. The circles indicate the depth of the downslope flow, calculated as the distance n along the normal at which the along-slope velocity component u_s decreases to 20 % of its maximum value, denoted by $u_{s,max}$. The dotted lines show horizontal lines. The dashed and straight solid lines mark the position of the top of the ground-based inversion layer and region of enhanced cooling, respectively. The dashed-dotted line indicates the location half-way along the slope. The curved solid line represents the depth of the downslope flow as inferred by $0.75\,E\,s$, where E is the entrainment coefficient and s is the along-slope distance from the top of the slope (see text for details). The plots below display $u_{s,max}$ (solid line), its distance along the normal $n(u_{s,max})$ (dashed line), the slope angle α (dotted line), the forcing terms F_i in the momentum budget for the tendency of u_s, averaged across the depth of the downslope flow, the cooling rate at the ground surface $\partial T_0/\partial t$, and the components Q_i (sensible heat Q_H, latent heat Q_E and conduction to the underlying soil Q_G) of the surface energy budget $R_n = Q_H + Q_E + Q_G + \Delta Q_S$, where $R_n = K^\star + L^\star$, $K^\star$ and $L^\star$ are net allwave, shortwave and longwave radiation, respectively, and ΔQ_S is the residual.

which represents changes of energy storage, is negative. This loss of energy results in a cooling at the surface (that is $\partial T_0/\partial t < 0$, where T_0 is the skin temperature). Even though $\partial T_0/\partial t$ is proportional to ΔQ_S at every time and point in the model domain, this is not necessarily the case when averaged along the valley axis.

The downslope flows accelerate or decelerate along the slopes as a result of the balance between the forcing terms in the momentum budget (see the middle plot in Fig. 2). Above the CAP, the dominant forcing mechanism is the buoyancy force, which is balanced mainly by the subgrid-scale (SGS) stress divergences (i.e., diffusion) and the advection terms. The most appropriate thermodynamics measure of the CAP top height (that is the height of the top of the humid layer) was determined following Burns and Chemel (2014b). Given the relatively large vertical height of the sloping surface ΔZ_s compared with the typical height scale of the flow H (yielding $\widehat{H} = H/\Delta Z_s \ll 1$) and the relatively small Froude number [$F = U^2/(g'H) < 1$, where U is the typical velocity scale of the flow and g' is the reduced gravity], this balance corresponds to the type of flow that Mahrt (1982) classified as a shooting flow. As the downslope flow penetrates into the CAP, the relative contribution of advection becomes less important. In this condition, the flow is classified as an equilibrium flow. This regime was reported in the numerical model experiments performed by Burkholder et al. (2009) over a steep slope with a constant slope angle of 20°. As the air flows down the slopes within the CAP, it reaches its level of neutral buoyancy and is detrained, largely above the ground-based inversion layer. The top height of the ground-based inversion layer was calculated as the level at which the temperature gradient reverses from positive to negative.

Cuxart et al. (2007) also reported the occurrence of shooting flows over a gentle (less than 2°) nearly two-dimensional slope on the island of Majorca, Balearic Islands, Spain, located in the western Mediterranean region, about 200 km off the Iberian peninsula. A mesoscale non-hydrostatic model was used to model one night in January 1999 at a horizontal resolution of 1 km and a vertical resolution adjacent to the ground surface of 3 m. Atmospheric microphysical processes were not considered. It was indicated that along approximately the first 5 km of the slope mountain waves perturbed the downslope flow, however, beyond this point the downslope flow existed in quiescent conditions. Beyond the 5-km mark the downslope evolution of the momentum budget (computed using a two-layer hydraulic model) during the early night generally follows the same pattern as that shown in Fig. 2. The increase in downslope flow depths, associated with the disruption of the downslope flows over the lower slopes, is evident in both sets of results. There is more variability in the momentum budget presented in Cuxart et al. (2007), which, at least partly, can be attributed to relatively abrupt changes in the slope angle (compared to the smoothly changing slope considered herein).

The top two plots of Fig. 2 show that the maximum speed of the downslope flow and the position of this maximum along the normal to the slope decrease with distance from the top of the slope within the CAP, while the depth of the flow is almost constant over the same section of slope above the ground-based inversion layer. Above the CAP, the depth of the flow follows closely that inferred (for neutral conditions) by $0.75Es$ (Manins and Sawford 1979), where E is the entrainment coefficient, estimated to be $0.05\,(\sin|\alpha|)^{2/3}$ (Briggs 1981) based on the data reported by Ellison and Turner (1959), where α is the slope angle, and s is the along-slope distance from the top of the slope. This entrainment process corresponds to the plume-like regime of downslope flows over steep slopes analyzed by Baines (2005). Within the CAP, the air above the downslope flow is not entrained but detrained, as indicated by the streamlines, and so the above semi-empirical estimation for the depth of the downslope flow is no longer appropriate.

The top plot in Fig. 2 shows the dispersion characteristics of the downslope flow. Consistent with results of numerical model simulations of tracer dispersion over a uniform slope with a constant slope angle of 20°analyzed by Nappo et al. (1989), pollutant P_1, released at ground-level on the plateaux, spreads through the entire depth of the downslope flow above the CAP. In this region there is a two-layer structure to the pollutant concentration within the downslope flow, essentially defined by the height of the cold-air jet maximum $n\,(u_{s,max})$. The two-layer thermal structure of the downslope flow was discussed more generally by Burns and Chemel (2014b). Figure 2 shows that above the CAP pollutant concentrations are higher below than above $n\,(u_{s,max})$. This indicates a near-decoupling of the air below the cold-air jet maximum from the air above it. Within the CAP the pollutant concentration within the downslope flow is nearly uniform. It seems reasonable to suggest that this is caused by relatively large oscillations of the downslope flow speed within the CAP, as shown by Burns and Chemel (2014b). These oscillations are likely to be associated with relatively intense mixing events, thereby mixing pollutants across the cold-air jet maximum. This is similar to an effect found by Cuxart and Jiménez (2007), who completed a LES of a cold-air jet over the Duero river basin on the Iberian peninsula, Spain. The cold-air jet, together with intermittent bursts of turbulence within the cold-air jet, were observed during the Stable Atmospheric Boundary Layer Experiment in Spain-1998 (SABLES-98; Cuxart et al. 2000). Good agreement between the LES results and the observations from SABLES-98 was found. Cuxart and Jiménez (2007) suggested that the mixing events could be explained by the 'Businger mechanism' (Businger 1973), which is different to that suggested to cause the change in pollutant dispersion shown in Fig. 2. However, this does not necessarily preclude the Businger mechanism from existing in the system considered herein.

Figure 2 shows that the concentration C_1' of pollutant P_1 decreases by an order of magnitude as the pollutant reaches the top of the CAP. As the pollutant penetrates into the CAP and flows down the slope within the CAP, it is mixed and detrained out of the downslope flow. The isopleths within the CAP show that concentrations are slightly higher above the ground-based inversion layer than below, indicating that some fraction penetrates into the ground-based inversion layer, despite its strong atmospheric stability.

To investigate the fate of the pollutants emitted along the slopes, Fig. 3 presents cross-valley vertical cross-sections of along-valley-averaged pollutant concentrations at the same time ($t = 480$ min). Pollutant P_{11}, emitted at the bottom of the slopes within the ground-based inversion layer, is largely trapped there (see Fig. 3f). Pollutant P_9, emitted farther up at the centre of the bottom half of the slopes (that is above the ground-based inversion layer), penetrates into the ground-based inversion layer, where its concentrations are highest, although some fraction detrains above it (see Fig. 3e). Pollutant P_7, emitted just below the top half of the slopes, detrains within the CAP and concentrates just above the ground-based inversion layer (see Fig. 3d). The pollutants emitted over the top half of the slopes display a similar behaviour to one another, with detrainment increasing with distance from the top of the slopes (see Fig. 3a to 3c). The concentrations of all pollutants above the CAP are relatively small with, at this time, no clear evidence of detrainment above the CAP top as defined by the top of the humid layer.

At that time ($t = 480$ min), an elevated inversion layer has developed close to the height of the plateaux, and the layer above the CAP is a region of increased atmospheric stability compared to the stability within the CAP (Burns and Chemel 2014b). As pointed out by Vergeiner and Dreiseitl (1987), an elevated inversion layer favours trapping. The argument is as follows: because of the enhanced atmospheric stability of the elevated inversion, the downslope flow mass flux is weaker in the elevated inversion than below. The airmass within the CAP is pushed up as the CAP grows, and when this airmass encounters the elevated

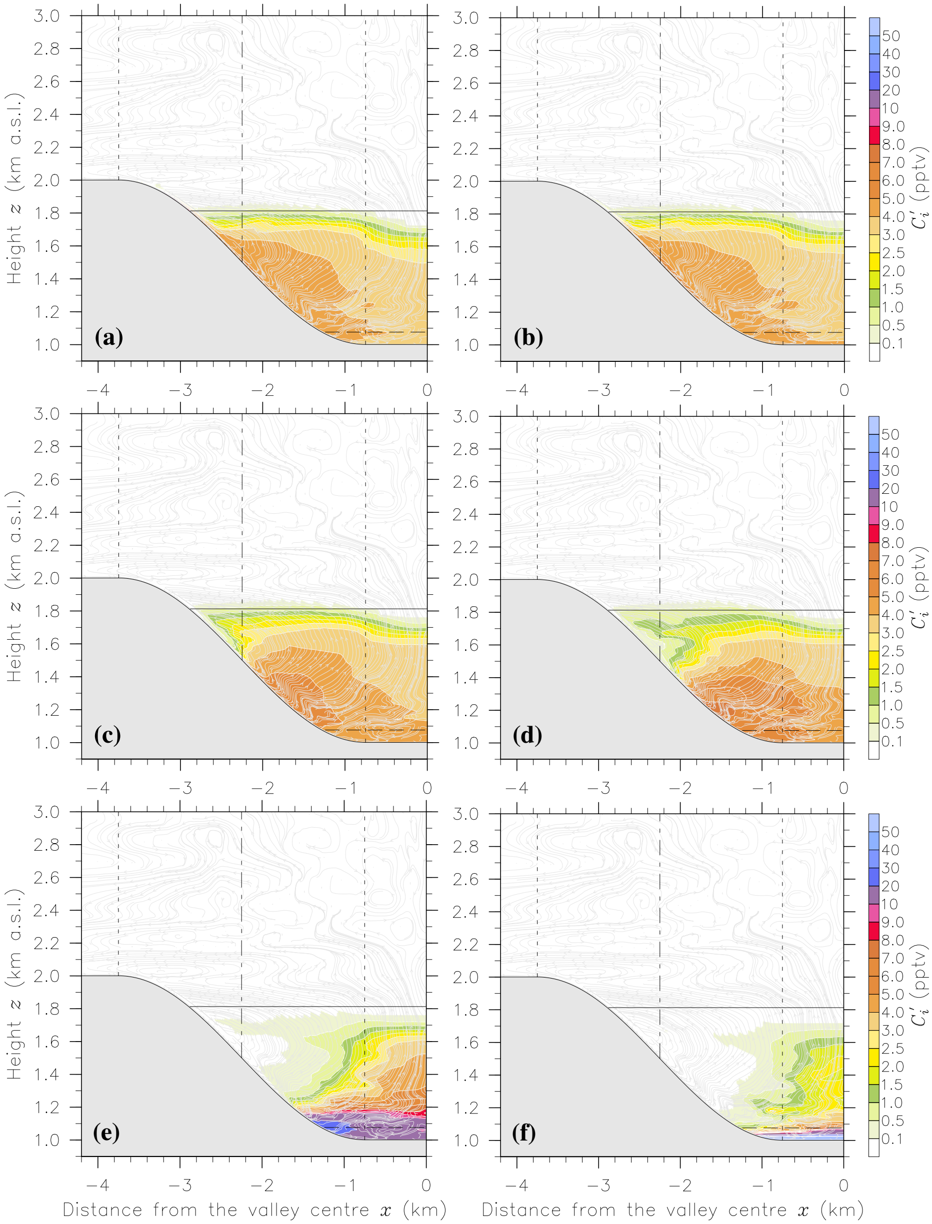

Fig. 3 Contour plots (**a**) to (**f**) of the along-valley-averaged concentration C_i' of pollutant P_i at time $t = 480$ min for $i = 2, 4, 6, 7, 9$ and 11, respectively, with streamlines superimposed. The horizontal dashed and solid lines mark the position of the top of the ground-based inversion layer and region of enhanced cooling, respectively. The vertical dotted lines mark the top and bottom of the western slope and the vertical dashed-dotted line indicates the location half-way along the slope.

inversion layer, it is transported towards the slopes at the lower boundary of the inversion layer, although some fraction is mixed within this layer.

The overview of the downslope flow, its forcing mechanisms and dispersion characteristics presented in this section calls for a quantification of the ability of the CAP to dilute pollutants, which is the purpose of the following section.

3.2 Dispersion characteristics of the developing CAP

Figure 4 shows time series of the along-valley- and hourly-averaged concentrations of each pollutant P_i, averaged between the ground and the top height of the ground-based inversion layer, denoted by $\langle C_i \rangle_{\mathrm{GBI}}$, averaged between the top height of the ground-based inversion layer and that of the CAP, denoted by $\langle C_i \rangle_{\mathrm{CAP}}$, and the slope winds averaged over the depth of the downslope flows and over the region of the slopes where pollutant P_i is emitted. The stepwise character of the time series is due to the algorithm used to track the positions of the top of the ground-based inversion layer and CAP (see Burns and Chemel 2014b). Once the flow is well established, about 1 h after sunset, the time evolutions of $\langle C_1 \rangle_{\mathrm{GBI}}$ and $\langle C_1 \rangle_{\mathrm{CAP}}$ follow closely those of the top height of the ground-based inversion layer and CAP, respectively. This shows that the downslope flows fill the valley with air from above, which is then trapped within the CAP.

The time evolution of the pollutant concentrations depends on where the pollutants are emitted with respect to the positions of the top of the ground-based inversion layer and CAP. Once the flow is well established, the concentrations of the pollutants emitted on the top half of the slopes (pollutants P_2 to P_6) are almost equal and constant with time, when averaged within the ground-based inversion layer, and almost equal but increasing steadily with time, when averaged within the CAP. The pollutants emitted towards the bottom of the slopes (pollutants P_9 to P_{12}) display a different behaviour. Their concentrations increase with time and distance from the top of the slopes, when averaged within the ground-based inversion layer, and decrease with time and distance from the top of the slopes, when averaged within the CAP.

Pollutants emitted within the ground-based inversion layer are largely trapped there. When pollutants are emitted at increasing distance above the ground-based inversion layer, their concentrations averaged within the ground-based inversion layer $\langle C_i \rangle_{\mathrm{GBI}}$, decrease because of dilution increasing with distance from their sources. More specifically, for the pollutants emitted over the lower part of the slopes $\langle C_i \rangle_{\mathrm{GBI}}$ is inversely proportional to the slope wind speeds where the pollutants are emitted, denoted by $\overline{u_s}|_i$. Since the slope wind speeds there decrease with distance from the top the slopes, this shows that the concentrations of these pollutants contain a factor proportional to the inverse of the distance from the sources, arising from 'plume' dispersion. This decrease in the slope wind speeds is due to their interaction with the growing CAP. The reader is referred to Burns and Chemel (2014b) for a detailed account of the influence of the developing CAP on the slope winds for the present simulation. The CAP-averaged concentrations $\langle C_i \rangle_{\mathrm{CAP}}$ are proportional to $\overline{u_s}|_i$ over the lower part of the slopes (pollutants P_9 to P_{12}), and diminish as the cold-air pool deepens.

Mahrt et al. (2010) also reported diminishing slope winds on clear nights over the gentle lower slope (with a slope angle of about 5°) of Tussey Ridge, Pennsylvania, USA. Near-surface observations, over the lowest 50 m of the approximately 300-m high ridge, indicated that the slope winds diminished to a light and variable condition as the night progressed, assumed to be due to the influence of the deepening CAP engulfing part of the slope.

The overall increase of $\langle C_{12} \rangle_{\mathrm{GBI}}$ during the early night generally reflects the trend of pollutant concentration at screen-level height over the valley floor (not shown). A general increase in benzene concentration during the first half of the night of 1 February 2006, ob-

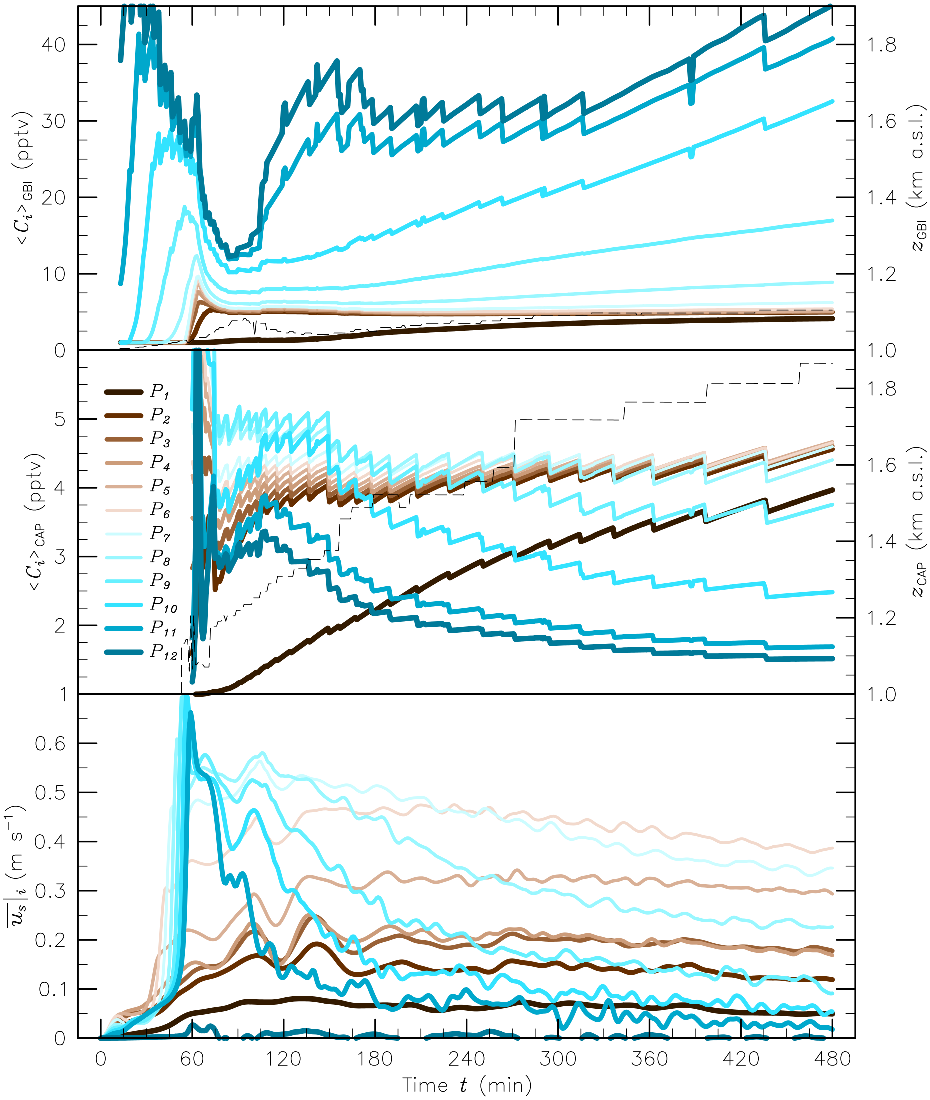

Fig. 4 Time series of the along-valley-averaged concentrations of pollutant P_i, $i \in [1..12]$, averaged between the ground and the top height of the ground-based inversion layer, denoted by $\langle C_i \rangle_{\mathrm{GBI}}$, averaged between the top height of the ground-based inversion layer and that of the region of enhanced cooling, denoted by $\langle C_i \rangle_{\mathrm{CAP}}$, and the slope winds averaged over the depth of the downslope flows and over the region of the slopes where pollutant P_i is emitted, denoted by $\overline{u_s}|_i$. The dashed lines in the top two plots indicate the top heights of the ground-based inversion layer z_{GBI} and region of enhanced cooling z_{CAP}.

served close to the floor of the Inn valley, Austria, was reported by Schnitzhofer et al. (2009). The Inn valley has a similar width and depth to the geometry considered herein, although is more complex with tributary valleys and frequent valley winds. The trend in benzene concentration noted above was observed during calm synoptic anticyclonic conditions with clear skies (except for scattered thin cirrus clouds). Wind speeds close to the ground were small (less than 1 m s^{-1}), although radiosonde data provided by Harnisch et al. (2009) suggest that a significant down-valley wind jet (maximum speed of approximately 7 m s^{-1}) existed about 400 m above the valley floor. Kitada and Regmi (2003) demonstrate the importance, in some cases, of valley and plain-to-mountain winds in the vertical and horizontal dispersion of air pollutants. Schnitzhofer et al. (2009) argued that the nocturnal increase in benzene concentrations was due to the development of a ground-based inversion layer, trapping pollutants close to the ground. In contrast to the observation of Schnitzhofer et al. (2009), Gohm et al. (2009) and Harnisch et al. (2009) provided data showing a general decrease in aerosol concentrations after sunset, observed on the same night and at the same location in the Inn valley. The trend in aerosol concentrations was in phase with that of vehicle numbers passing through the area. This suggests that the evolution of emissions and/or chemistry can be as important in controlling concentrations as the evolution of near-ground static stability. It is worth noting that shorter-term reductions (about an hour) are evident in $\langle C_{12}\rangle_{\mathrm{GBI}}$ (e.g. close to $t = 180$ min); a result of the interactions between the downslope winds and the ground-based inversion layer.

Figure 5 presents vertical profiles of hourly-averaged pollutant concentrations, averaged across the valley floor, away from the slopes. The profiles show a marked build-up of pollution within about 100 m above the valley floor for the pollutants emitted towards the bottom of the slopes (pollutants P_9, P_{11} and P_{12}), which are engulfed by the ground-based inversion layer. Their concentrations decrease sharply with height across the ground-based inversion layer. The pollutants emitted farther up the slopes are almost well mixed within the CAP, suggesting detrainment through the entire depth of the CAP, as can be seen in Figs. 2 and 3. This well-mixed behaviour is also promoted by the slow decrease in atmospheric stability of the CAP above the ground-based inversion layer, once the flow is well established (about 1 h after sunset), from about 8 K km^{-1} (i.e., a value about 5 to 6 times larger than at the start of the simulation) to about 5 K km^{-1} at the end of the simulated 8-h period (Burns and Chemel 2014b). Pollutant P_1, emitted on the plateaux, is less concentrated within the CAP than the pollutants emitted at the top of the slopes, indicating that the downslope flows do not draw air only from the plateaux but also entrain air from above the slopes.

Table 1 reports measures of the dilution of each pollutant within the developing CAP. The ratio $\langle C_{i,1}\rangle_{\mathrm{f}}/C_{i,max}$, where $\langle C_{i,1}\rangle_{\mathrm{f}}$ is the hourly-averaged concentration of pollutant P_i, averaged across the valley floor, within the model layer adjacent to the ground surface and $C_{i,max}$ is the maximum hourly-averaged concentration of pollutant P_i within the model domain (almost constant over time). This ratio is a measure of the overall dilution from the emission sources to the valley floor. This ratio generally decreases with time for all the pollutants [except those emitted at the very top of the slopes (pollutants P_1 to P_3)]. Over time the pollutants are mixed through and out of the ground-based inversion layer. Unexpected increases and decreases of this ratio are noted from $t = 120$ to 240 min, which is approximately the time when the top of the CAP reaches the height of the strongest slope winds (see Burns and Chemel 2014b, for details of the complex interactions between the downslope flows and the developing CAP). For pollutant P_{12}, emitted at the valley floor, the ratio is less than 100 %, indicating that its concentration is not uniform across the valley floor, and consistent with pollutants being lifted up at the centre of the valley, as discussed above. The dilution from the emission sources is found to be inversely proportional to the slope wind speeds where the pollutants are emitted, as can be seen in Figs. 2 and 4. At the end of the simulated 8-h period, the concentration of the pollutants emitted on the steepest slopes, where the slope winds are the strongest, is about 40 % smaller at the valley floor than at the emission source.

The ratio $\langle C_{i,\mathrm{GBI}}\rangle_{\mathrm{f}}/\langle C_{i,1}\rangle_{\mathrm{f}}$, where $\langle C_{i,\mathrm{GBI}}\rangle_{\mathrm{f}}$ is the hourly-averaged concentration of pollutant P_i, averaged across the valley floor, at the top height of the ground-based inversion

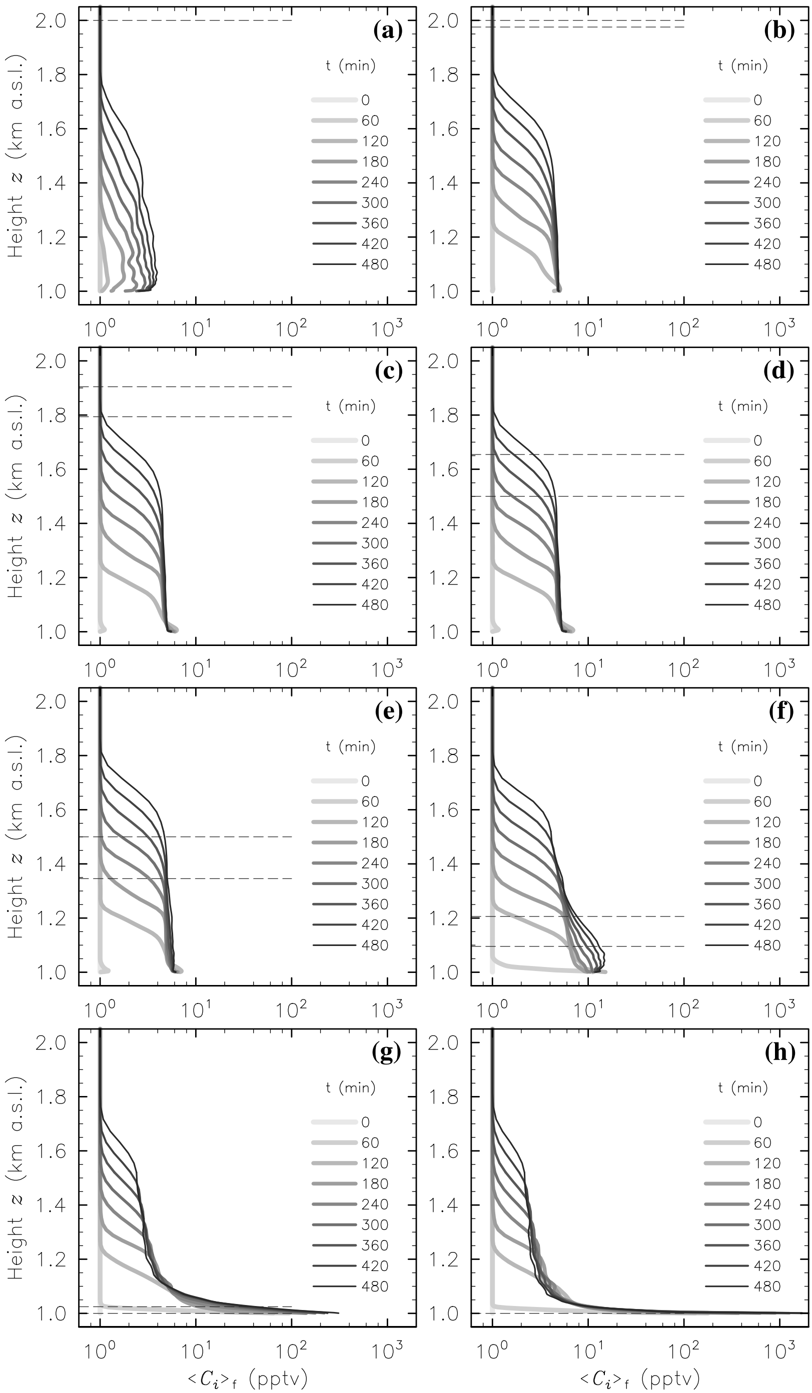

Fig. 5 Vertical profiles (**a**) to (**h**) of the hourly-averaged concentration of pollutant P_i, averaged across the valley floor, denoted by $\langle C_i \rangle_\mathrm{f}$, at times $t = 0, 60, 120, 180, 240, 300, 360, 420$ and 480 min for $i = 1, 2, 4, 6, 7, 9, 11$ and 12, respectively. The dashed lines mark the boundaries of the height range over which the pollutant P_i is emitted.

Table 1 Ratios $\langle C_{i,1}\rangle_{\mathrm{f}}/C_{i,max}$, $\langle C_{i,\mathrm{GBI}}\rangle_{\mathrm{f}}/\langle C_{i,1}\rangle_{\mathrm{f}}$ and $\langle C_{i,\mathrm{CAP}}\rangle_{\mathrm{f}}/\langle C_{i,1}\rangle_{\mathrm{f}}$, for pollutants P_i, $i \in [1..12]$, at times $t =$ 120, 240, 360, 420 and 480 min, where $\langle C_{i,1}\rangle_{\mathrm{f}}$, $\langle C_{i,\mathrm{GBI}}\rangle_{\mathrm{f}}$ and $\langle C_{i,\mathrm{CAP}}\rangle_{\mathrm{f}}$ are the hourly-averaged concentrations of pollutant P_i, averaged across the valley floor, within the model layer adjacent to the ground surface, at the top height of the ground-based inversion layer and at the top of the cold-air pool, respectively, and $C_{i,max}$ is the maximum hourly-averaged concentration of pollutant P_i within the model domain

t (min)	P_1	P_2	P_3	P_4	P_5	P_6	P_7	P_8	P_9	P_{10}	P_{11}	P_{12}
$(\langle C_{i,1}\rangle_{\mathrm{f}}/C_{i,max}) \times 100$ (%)												
120	0.4	2.9	9.2	35.9	54.5	67.8	72.1	88.8	76.5	80.0	56.9	65.4
240	0.5	4.7	23.7	44.7	57.6	62.5	59.2	54.3	44.2	39.2	46.0	76.1
360	0.8	5.1	24.8	42.6	51.8	53.3	48.3	41.2	33.5	31.0	29.2	72.6
480	0.8	5.1	24.7	39.7	47.7	47.8	43.1	35.4	20.9	16.7	18.0	82.5
$(\langle C_{i,\mathrm{GBI}}\rangle_{\mathrm{f}}/\langle C_{i,1}\rangle_{\mathrm{f}}) \times 100$ (%)												
120	113.6	86.9	76.6	74.0	73.0	72.6	73.8	66.6	48.5	23.9	11.0	4.7
240	123.4	93.4	84.1	80.4	78.2	77.4	79.0	78.2	73.4	42.3	4.4	0.8
360	119.9	95.9	89.1	86.2	84.5	84.1	86.3	88.1	84.0	36.0	2.6	0.3
480	144.3	98.2	91.5	88.6	86.9	87.4	93.2	102.8	107.3	41.5	1.7	0.2
$(\langle C_{i,\mathrm{CAP}}\rangle_{\mathrm{f}}/\langle C_{i,1}\rangle_{\mathrm{f}}) \times 100$ (%)												
120	97.1	30.0	25.9	24.6	23.8	23.4	23.8	19.4	11.5	4.6	2.0	1.0
240	54.6	20.4	18.5	17.7	17.1	16.6	16.4	14.0	9.7	4.4	0.7	0.2
360	39.5	20.4	18.9	18.2	17.6	17.1	16.4	13.5	8.5	3.3	0.4	0.1
480	38.9	20.7	19.3	18.6	18.0	17.5	16.7	13.5	8.4	3.1	0.3	0.0

layer, is a measure of the overall vertical dilution within the ground-based inversion layer. This ratio generally increases with time for all the pollutants, except those emitted at the very bottom of the slopes (pollutants P_{10} to P_{12}). This shows that the gradient of concentration decreases over time, suggesting a build-up of pollution above the ground-based inversion layer, which is increasingly mixed over time, as noted above. The concentrations of the pollutants emitted within the ground-based inversion layer decrease sharply with height. For example, the concentration of pollutant P_{12} decreases by almost two orders of magnitude from the valley floor to the top of the ground-based inversion layer.

The ratio $\langle C_{i,\mathrm{CAP}}\rangle_{\mathrm{f}}/\langle C_{i,1}\rangle_{\mathrm{f}}$, where $\langle C_{i,\mathrm{CAP}}\rangle_{\mathrm{f}}$ is the hourly-averaged concentration of pollutant P_i, averaged across the valley floor, at the top of the CAP, is a measure of the overall vertical dilution within the CAP. This ratio depends on where the pollutants are emitted with respect to the positions of the top of the ground-based inversion layer and CAP, and on the slope wind speeds, as for $\langle C_i\rangle_{\mathrm{GBI}}$ and $\langle C_i\rangle_{\mathrm{CAP}}$ (see Fig. 4). It generally increases with time for the pollutants emitted on the top half of the slopes (pollutants P_2 to P_6) and decreases with time for the pollutants emitted on the bottom half of the slopes (pollutants P_7 to P_{11}). This is explained as follows: the pollutants emitted within the ground-based inversion layer are largely trapped there. The pollutants emitted farther up the slopes detrain within the CAP above the ground-based inversion layer, although some fraction, increasing with distance from the top of the slopes, penetrates into the ground-based inversion layer.

4 Summary

The purpose of our study was to quantify the role of cold-air-pooling processes in the dispersion of air pollution in the developing valley cold-air pool studied by Burns and Chemel (2014a,b). The key findings are summarized below.

- The overview of the downslope flow, its forcing mechanisms and dispersion characteristics presented in Sect. 3.1 showed that the negatively buoyant downslope flows transport and mix pollutants into the valley to depths that depend on the temperature deficit of the flow and the ambient temperature structure inside the valley. Along the slopes, pollutants are generally entrained above the cold-air pool and detrained within the cold-air pool, largely above the ground-based inversion layer.
- The ability of the cold-air pool to dilute pollutants was quantified in Sect. 3.2. The analysis indicated that the downslope flows fill the valley with air from above, which is then trapped within the cold-air pool, and that the air is drawn not only from the plateaux but also from above the slopes. Once the flow is well established, about 1 h after sunset, the pollutants within the ground-based inversion layer are continuously replenished by the downslope flows, despite its strong atmospheric stability. Dilution depends on where the pollutants are emitted with respect to the positions of the top of the ground-based inversion layer and cold-air pool, and on the slope wind speeds. Over the lower part of the slopes, the cold-air-pool-averaged concentrations are proportional to the slope wind speeds where the pollutants are emitted, and diminish as the cold-air pool deepens. Pollution accumulates within the ground-based inversion layer for the pollutants emitted towards the bottom of the slopes, which are engulfed by the ground-based inversion layer. Their concentrations decrease sharply with height across the ground-based inversion layer. The concentration of the pollutant emitted on the valley floor decreases by almost two orders of magnitude from the valley floor to the top of the ground-based inversion layer by the end of the simulated 8-h period. The pollutants emitted farther up the slopes detrain within the CAP above the ground-based inversion layer, although some fraction, increasing with distance from the top of the slopes, penetrates into the ground-based inversion layer. The concentration of the pollutants emitted on the steepest slopes, where the slope winds are the strongest, is about 40 % smaller at the valley floor than at the emission source at the end of the simulated 8-h period.

The results presented herein have important practical implications for the assessment and management of pollution in the atmosphere and in other fluid analogues. It is hoped that the present work will provide an impetus to investigate pollutant dispersion in cold-air pools.

References

Baines PG (2005) Mixing regimes for the flow of dense fluid down slopes into stratified environments. J Fluid Mech 538:245–267

Baker KR, Simon H, Kelly JT (2011) Challenges to modeling "cold pool" meteorology associated with high pollution episodes. Environ Sci Technol 45:7118–7119

Briggs GA (1981) Canopy effects on predicted drainage flow characteristics and comparison with observations. In: Proc. of the Fifth AMS Symposium on Turbulence and Diffusion, Atlanta, GA, USA, American Meteorological Society, Boston, MA, USA, pp 113–115

Brulfert C, Chemel C, Chaxel E, Chollet JP (2005) Modelling photochemistry in alpine valleys. Atmos Chem Phys 5:2341–2355

Burkholder BA, Shapiro A, Fedorovich E (2009) Katabatic flow induced by a cross-slope band of surface cooling. Acta Geophys 57:923–949

Burns P, Chemel C (2014a) Evolution of cold-air-pooling processes in complex terrain. Boundary-Layer Meteorol 150:423–447

Burns P, Chemel C (2014b) Interactions between downslope flows and a developing cold-air pool. Boundary-Layer Meteorol DOI 10.1007/s10546-014-9958-7, in press

Businger JA (1973) Turbulent transfer in the atmospheric surface layer. In: Haugen DA (ed) Proc. of the Workshop on Micrometeorology, Boston, MA, USA, American Meteorological Society, Boston, MA, USA, pp 67–100

Chazette P, Couvert P, Randriamiarisoa H, Sanak J, Bonsang B, Moral P, Berthier S, Salanave S, Toussaint F (2005) Three-dimensional survey of pollution during winter in French Alps valleys. Atmos Environ 39:1035–1047

Chen F, Dudhia J (2001) Coupling an advanced land-surface/hydrology model with the Penn State/NCAR MM5 modeling system. Part I: model implementation and sensitivity. Mon Weather Rev 129:569–585

Cuxart J, Jiménez MA (2007) Mixing processes in a nocturnal low-level jet: an LES study. J Atmos Sci 64:1666–1679

Cuxart J, Jiménez MA (2012) Deep radiation fog in a wide closed valley: study by numerical modeling and remote sensing. Pure Appl Geophys 169:911–926

Cuxart J, Yagüe C, Morales G, Terradellas E, Orbe J, Calvo J, Fernández A, Soler MR, Infante C, Buenestado P, Espinalt A, Joergensen HE, Rees JM, Vilá J, Redondo JM, Cantalapiedra IR, Conangla L (2000) Stable Atmospheric Boundary-Layer Experiment in Spain (SABLES-98): a report. Boundary-Layer Meteorol 96:337–370

Cuxart J, Jiménez MA, Martínez D (2007) Nocturnal meso-beta basin and katabatic flows on a midlatitude island. Mon Weather Rev 135:918–932

de Franceschi M, Zardi D (2009) Study of wintertime high pollution episodes during the Brenner-South ALPNAP measurement campaign. Meteorol Atmos Phys 103:237–250

Deardorff JW (1980) Stratocumulus-capped mixed layers derived from a three-dimensional model. Boundary-Layer Meteorol 18:495–527

Dorninger M, Whiteman CD, Bica B, Eisenbach S, Pospichal B, Steinacker R (2011) Meteorological events affecting cold-air pools in a small basin. J Appl Meteorol Climatol 50:2223–2234

Dudhia J (1995) Reply. Mon Weather Rev 123:2573–2575

Ellison TH, Turner JS (1959) Turbulent entrainment in stratified flows. J Fluid Mech 6:423–448

Gohm A, Harnisch F, Vergeiner J, Obleitner F, Schnitzhofer R, Hansel A, Fix A, Neininger B, Emeis S, Schäfer K (2009) Air pollution transport in an alpine valley: results from airborne and ground-based observations. Boundary-Layer Meteorol 131:441–463

Haiden T, Whiteman DC, Hoch SW, Lehner M (2011) A mass flux model of nocturnal cold-air intrusions into a closed basin. J Appl Meteorol Climatol 50:933–943

Harnisch F, Gohm A, Fix A, Schnitzhofer R, Hansel A, Neininger B (2009) Spatial distribution of aerosols in the Inn Valley atmosphere during wintertime. Meteorol Atmos Phys 103:223–235

Hoch SW, Whiteman DC, Mayer B (2011) A systematic study of longwave radiative heating and cooling within valleys and basins using a three-dimensional radiative transfer model. J Appl Meteorol Climatol 50:2473–2489

Jiménez PA, Dudhia J, Gonzalez-Rouco JF, Navarro J, Montávez JP, García-Bustamante E (2012) A revised scheme for the WRF surface layer formulation. Mon Weather Rev 140:898–918

King JA, Shair FH, Reible DD (1987) The influence of atmospheric stability on pollutant transport by slope winds. Atmos Environ 21:53–59

Kitada T, Regmi RP (2003) Dynamics of air pollution transport in late wintertime over Kathmandu valley, Nepal: as revealed with numerical simulation. J Appl Meteorol 42:1770–1798

Klemp JB, Dudhia J, Hassiotis AD (2008) An upper gravity-wave absorbing layer for NWP applications. Mon Weather Rev 136:3987–4004

Lareau NP, Horel JD (2014) Dynamically induced displacements of a persistent cold-air pool. Boundary-Layer Meteorol DOI 10.1007/s10546-014-9968-5, in press

Lee SM, Fernando HJS, Princevac M, Zajic D, Sinesi M, McCulley JL, Anderson J (2003) Transport and diffusion of ozone in the nocturnal and morning planetary boundary layer of the Phoenix valley. Environ Fluid Mech 3:331–362

Lehner M, Gohm A (2010) Idealised simulations of daytime pollution transport in a steep valley and its vensitivity to thermal stratification and surface albedo. Boundary-Layer Meteorol 134:327–351

Mahrer Y (1984) An improved numerical approximation of the horizontal gradients in a terrain-following coordinate system. Mon Weather Rev 112:918–922

Mahrt L (1982) Momentum balance of gravity flows. J Atmos Sci 39:2701–2711

Mahrt L, Richardson S, Seaman N, Stauffer D (2010) Non-stationary drainage flows and motions in the cold pool. J Atmos Sci 62A:698–705

Malek E, Davis T, Martin RS, Silva PJ (2006) Meteorological and environmental aspects of one of the worst national air pollution episodes (January, 2004) in Logan, Cache Valley, Utah, USA. Atmos Research 79:108–122

Manins PC, Sawford BL (1979) A model of katabatic winds. J Atmos Sci 36:619–630

Martínez D, Cuxart J (2009) Assessment of the hydraulic slope flow approach using a mesoscale model. Acta Geophys 57:882–903

Martínez D, Jiménez MA, Cuxart J (2010) Heterogeneous nocturnal cooling in a large basin under very stable conditions. Boundary-Layer Meteorol 137:97–113

McKee TB, O'Neal RD (1988) The role of valley geometry and energy budget in the formation of nocturnal valley winds. J Appl Meteorol 28:445–456

Moeng CH, Dudhia J, Klemp J, Sullivan P (2007) Examining two-way grid nesting for large eddy simulation of the PBL using the WRF model. Mon Weather Rev 135:2295–2311

Nappo CJ, Rao KS, Herwehe JA (1989) Pollutant transport and diffusion in katabatic flows. J Appl Meteorol 28:617–625

Raga GB, Baumgardner D, Kok G, Rosas I (1999) Some aspect of boundary layer evolution in Mexico City. Atmos Environ 33:5013–5021

Schnitzhofer R, Norman M, Wisthaler A, Vergeiner J, Harnisch F, Gohm A, Obleitner F, Fix A, Neininger B, Hansel A (2009) A multimethodological approach to study the spatial distribution of air pollution in an alpine valley during wintertime. Atmos Chem Phys 9:3385–3396

Scotti A, Meneveau C, Lilly DK (1993) Generalized Smagorinsky model for anisotropic grids. Phys Fluids 5:2306–2308

Silcox GD, Kelly KE, Crosman ET, Whiteman CD, Allen BL (2012) Wintertime $PM_{2.5}$ concentrations during persistent, multi-day cold-air pools in a mountain valley. Atmos Environ 46:17–24

Skamarock WC, Klemp JB, Dudhia J, Gill DO, Barker DM, Duda MG, Huang XY, Wang W, Powers JG (2008) A Description of the Advanced Research WRF Version 3. NCAR Technical Note NCAR/TN-475+STR, NCAR, Boulder, CO, USA, 125 pp

Vergeiner I, Dreiseitl E (1987) Valley winds and slope winds – Observations and elementary thoughts. Meteorol Atmos Phys 36:264–286

Vosper SB, Brown AR (2008) Numerical simulations of sheltering in valleys: the formation of nighttime cold-air pools. Boundary-Layer Meteorol 127:429–448

Vosper SB, Hughes JK, Lock AP, Sheridan PF, Ross AN, Jemmett-Smith B, Brown AR (2014) Cold-pool formation in a narrow valley. Q J R Meteorol Soc 140:699–714

Whiteman CD (2000) Mountain Meteorology: fundamentals and applications. Oxford University Press, New York, NY, USA, 355 pp

Whiteman CD, Zhong S (2008) Downslope flows on a low-angle slope and their interactions with valley inversions. Part I: observations. J Appl Meteorol Climatol 47:2023–2038

Whiteman CD, Zhong S, Bian X (1997) Wintertime boundary layer structure in the Grand Canyon. J Appl Meteorol 38:1084–1102

Whiteman CD, De Wekker SFJ, Haiden T (2007) Effect of dewfall and frostfall on nighttime cooling in a small, closed basin. J Appl Meteorol Climatol 46:3–13

Whiteman CD, Hoch SW, Lehner M (2010) Nocturnal cold-air intrusions into a closed basin: observational evidence and conceptual model. J Appl Meteorol Climatol 49:1894–1905

Zardi D, Whiteman CD (2013) Diurnal mountain wind systems. In: Chow FK, De Wekker SFJ, Snyder BJ (eds) Mountain Weather Research and Forecasting: Recent Progress and Current Challenges, Springer Atmospheric Sciences, Springer, New York, NY, USA, chap 2, pp 35–119